Clinical Neurophysiology 130 (2019) 2114–2123

Contents lists available at ScienceDirect

Clinical Neurophysiology

journal homepage: www.elsevier.com/locate/clinph

Novel functional imaging technique for the brachial plexus based on magnetoneurography

Taishi Watanabe [a,b], Shigenori Kawabata [c,*], Yuko Hoshino [c], Shuta Ushio [a], Toru Sasaki [a], Yuki Miyano [b], Isamu Ozaki [d], Yoshiaki Adachi [e], Kensuke Sekihara [c], Atsushi Okawa [a]

[a] *Department of Orthopedic Surgery, Tokyo Medical and Dental University, 1-5-45 Yushima, Bunkyo-ku, Tokyo 113-8510, Japan*
[b] *Healthcare Business Groupe, RICOH Company, Ltd., 2-3-10 Kandasurugadai, Chiyoda-ku, Tokyo 101-0062, Japan*
[c] *Department of Advanced Technology in Medicine, Graduate School of Tokyo Medical and Dental University, 1-5-45 Yushima, Bunkyo-ku, Tokyo 113-8510, Japan*
[d] *Faculty of Health Sciences, Aomori University of Health and Welfare, 58-1 Mase, Hamadate, Aomori-shi, Aomori 030-8505, Japan*
[e] *Applied Electronics Laboratory, Kanazawa Institute of Technology, Kanazawa-shi, Ishikawa 920-1331, Japan*

ARTICLE INFO

Article history:
Accepted 12 August 2019
Available online 22 August 2019

Keywords:
Magnetoneurography
Evoked magnetic field
Brachial plexus
Median nerve
Ulnar nerve
Conduction velocity

HIGHLIGHTS

- Neural activity in the brachial plexus can be visualized by magnetoneurography.
- Conductions in response to median and ulnar nerve stimulations can be differentiated.
- Currents flowing into the depolarization site can be computationally reconstructed.

ABSTRACT

Objective: To visualize neural activity in the brachial plexus using magnetoneurography (MNG).
Methods: Using a 124- or 132-channel biomagnetometer system with a superconducting quantum interference device, neuromagnetic fields above the clavicle and neck region were recorded in response to electrical stimulation of the median and ulnar nerves in five asymptomatic volunteers (four men and one woman; age, 27–45 years old). Equivalent currents were computationally reconstructed from neuromagnetic fields and visualized as pseudocolor maps. Reconstructed currents at the depolarization site and compound nerve action potentials (CNAPs) at Erb's point were compared.
Results: Neuromagnetic fields were recorded in all subjects. The reconstructed equivalent currents propagated into the vertebral foramina, and the main inflow levels differed between the median nerve (C5/C6–C7/T1 vertebral foramen) and the ulnar nerve (C7/T1–T1/T2). The inward current peaks at the depolarization site and CNAPs showed high linear correlation.
Conclusions: MNG visualizes neural activity in the brachial plexus and can differentiate the conduction pathways after median and ulnar nerve stimulations. In addition, it can visualize not only the leading and trailing components of intra-axonal currents, but also inward currents at the depolarization site.
Significance: MNG is a novel and promising functional imaging modality for the brachial plexus.

1. Introduction

Imaging and functional studies, as well as physical examination including various provocation tests, are essential for evaluating brachial plexus disorders due to trauma, entrapment, tumors, and other causes. The brachial plexus is highly susceptible to trauma and other diseases because of its superficial location and its position between highly mobile structures, the neck and the arm (Ferrante, 2012). Nevertheless, assessment of brachial plexus pathology has been challenging due to its anatomical features:

Abbreviations: CMAP, compound muscle action potential; CNAP, compound nerve action potential; MNG, magnetoneurography; SEP, somatosensory evoked potential; SNAP, sensory nerve action potential; SQUID, superconducting quantum interference device; UGRENS, unit gain constraint recursively applied null-steering spatial filtering.

* Corresponding author. Fax: +81 3 5803 5281.

E-mail addresses: taishi.watanabe@jp.ricoh.com (T. Watanabe), kawabata.orth@tmd.ac.jp (S. Kawabata), hoshino.atm@tmd.ac.jp (Y. Hoshino), ushio.orth@tmd.ac.jp (S. Ushio), t-sasaki.orth@tmd.ac.jp (T. Sasaki), yuki.yh.hasegawa@jp.ricoh.com (Y. Miyano), isamu@auhw.ac.jp (I. Ozaki), okawa.orth@tmd.ac.jp (A. Okawa).

https://doi.org/10.1016/j.clinph.2019.08.006

its position running though the muscles and bones of the shoulder and neck and the variety of its neural components.

In brachial plexus injury, imaging and electrophysiological studies are used for the localization and characterization of the lesion, for diagnosis, and for determination of surgical options (Ferrante, 2012; Giuffre et al., 2010; O'Shea et al., 2011). They also help to assess the nerve components involved. The location of the lesion, such as pre- or postganglionic, affects the neurophysiological study results and the treatment options.

As for electrophysiological examination of the brachial plexus, the modalities that can be used include sensory nerve action potential (SNAP), somatosensory evoked potential (SEP), needle electromyography, and compound muscle action potential (CMAP). Although these are helpful modalities for diagnosis and pre- and post-operative studies, they have some limitations. For example, the SNAP and CMAP may be normal soon after acute postganglionic nerve injury unless Wallerian degeneration occurs. In preganglionic injury of the sensory nerve, the SNAP remains intact without combined distal lesions. Similarly, a concurrent preganglionic lesion cannot be denied even in the case of postganglionic injury.

Imaging techniques such as X-ray imaging, ultrasonography, CT myelography, and magnetic resonance imaging are useful to detect the nerve lesion location and any concurrent bony and soft tissue injuries (Caranci et al., 2013; Marquez Neto et al., 2017; Rehman et al., 2014). Differentiation of the complete discontinuation of an axon (axonotmesis or neurotmesis) from neurapraxia is clinically important when considering the indication for surgical treatment. Although most traditional imaging techniques are unable to detect axon loss, diffusion tensor imaging has the potential to reveal axonal discontinuation or regeneration (Marquez Neto et al., 2017; Simon et al., 2016).

While the combination of physical examination and imaging and electrophysiological studies is helpful and reliable in most cases, the interpretation of these results is sometimes difficult for non-specialists. To create true benefit for patients, a functional imaging method that is easily comprehensible for physicians from diverse backgrounds is desired. Magnetoneurography (MNG) has the potential to be one such functional imaging method.

MNG is a functional imaging modality that detects magnetic fields generated by electric activity in nerves. Magnetoencephalography and magnetocardiography obtain biomagnetic recordings and are already available for clinical use. MNG for the spinal cord and peripheral nerves is now being developed for clinical application, and pioneering studies have been reported (Curio et al., 1991; Hashimoto et al., 1991; Hoshiyama et al., 1999; Klein et al., 2006; Mackert, 2004; Mackert et al., 2001a, 2000, 2001b, 1997, 1998; Trahms et al., 1989; Wijesinghe, 2010, 2014; Wijesinghe and Roth, 2009; Wikswo et al., 1980).

Our group has developed the system for MNG and magnetospinography and reported the visualization of neural activities in peripheral nerves and the spinal cord in both animals and humans (Fukuoka et al., 2004, 2002; Hoshino et al., 2005; Ishii et al., 2012; Kawabata et al., 2002; Ohkubo et al., 2003; Sumiya et al., 2017; Tomizawa et al., 2008; Tomori et al., 2010; Ushio et al., 2019). One notable advantage of MNG is that it can computationally reconstruct equivalent currents and visualize electrical activity. Although even normal electrical neural activity attenuates along conduction, MNG may be able to detect nerve lesions in the conduction pathway from the peripheral nerve to the spinal cord, including the brachial plexus. We previously reported that MNG is clinically useful for examining electrical activity in the spinal cord and the corda equina (Ishii et al., 2012; Ushio et al., 2019). However, the validity of MNG for assessing the brachial plexus remained unclear.

In this study, we present a visualization of electrical activity along the brachial plexus using our MNG system, including reconstructed currents flowing into the depolarization site. In addition, we consider the clinical application of MNG as a functional imaging method for the brachial plexus.

2. Methods

2.1. MNG system

Biomagnetic recordings were performed in a magnetically shielded room with a 124- or 132-channel SQUID biomagnetometer system developed by Kanazawa Institute of Technology and RICOH Company, Ltd. (Adachi et al., 2017, 2009, 2007, 2011, 2013). The system has 44 vector-type SQUID magnetic sensors arranged in a 180-mm × 130-mm area along the cylindrical surface with a radius of 200 mm (Fig. 1). In the 124-channel system, the sensors at the four corners recorded magnetic fields only in the Z direction owing to the restrictions of the electronic circuit. Positive in the X direction was set to be from the left to the right of the body, in the Y direction from caudal to cranial, and in the Z direction from the dorsal to the ventral side of the body.

2.2. Positional information

Two X-ray irradiation devices were installed above and beside the sensor array to take an X-ray image of the subjects in the measurement position (Fig. 1a). Marker coils were placed under the subjects and the relative position to the person was acquired in the anteroposterior view of the X-ray image. Magnetic fields generated by the marker coils were recorded before measurement of the subjects, and the relative position of the marker coils to the sensor array was estimated (Erne et al., 1987). The position of the subject on the measurement area was obtained from the information described above.

2.3. Subjects and recording of neuromagnetic fields and compound nerve action potentials

The subjects were five asymptomatic volunteers (four men and one woman; age, 27–45 years old; height, 164–175 cm). Neuromagnetic fields and compound nerve action potentials (CNAPs) were recorded in response to electrical stimulation of the median and ulnar nerves, respectively. In a magnetically shielded room, the subjects were prone on a table with the right arm pronated. The measurement area was arranged so as to cover the region from the anterior neck to the coracoid process (Fig. 2). The nerve was electrically stimulated at the wrist (square wave pulse, 5 Hz; 0.3 ms in duration) with supramaximal intensity that evoked maximal CNAP at Erb's point (6–12 mA in intensity). Evoked magnetic fields were recorded by the MNG system using a 40-kHz sampling rate and 100–5000-Hz bandpass filter, and 2000 responses were averaged (Fig. 3).

The CNAPs at Erb's point were measured in the same position using a MEB-2312 system (Nihon Kohden Corporation, Japan) with a 10-kHz sampling rate, 20–2000-Hz bandpass filter, and the average of 1000 responses.

All procedures in this study were approved by the Ethics Committee of Tokyo Medical and Dental University and carried out in accordance with the Declaration of Helsinki. We obtained written informed consent and releases for images and photographs from all subjects.

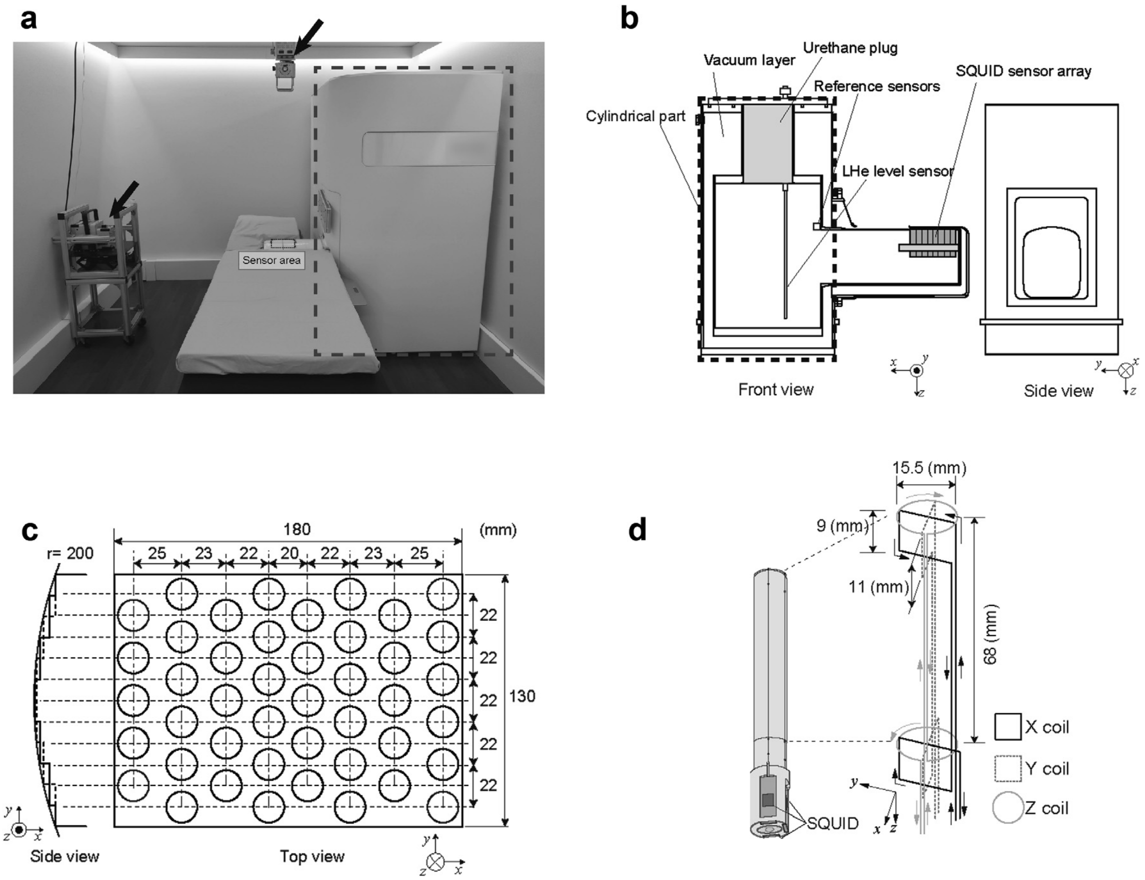

Fig. 1. Appearance and structure of the MNG system. (a) Appearance of the 124- or 132-channel SQUID biomagnetometer system in a magnetically shielded room. The cryostat has a protrusion on the side surface of the cylindrical main body contained in the housing indicated by the black dotted square. The protrusion holds the SQUID sensor array in the sensor area indicated by the black dotted square. Two X-ray irradiation devices (black arrows) were installed to take posteroanterior and lateral X-ray images of the subject and the sensors in the measurement position. (b) Inner structure and dimensions of the cryostat. The cylindrical part was placed in the housing indicated by the black dotted square. The right side of the red dotted line is the protrusion holding the SQUID sensors. (c) An array of 44 SQUID vector gradiometers with a matrix-like arrangement. In a 124-channel SQUID biomagnetometer system, the four sensors placed at the four corners are axial-type SQUID gradiometers for recording magnetic fields only in the Z direction. The other 40 sensors are vector-type SQUID gradiometers, which are equipped with two planar-type gradiometric pickup coils and an axial type for recording signals. (d) Structure of the vector-type SQUID gradiometers. Each sensor is equipped with two planar-type gradiometric pickup coils and an axial-type gradiometric pickup coil combined into one bobbin. Each pickup coil is oriented perpendicularly to each other and connected to an individual SQUID to simultaneously detect the three independent components of magnetic fields. The baseline length of each gradiometric pickup coil is 68 mm and the noise level was less than 4 fT/Hz$^{0.5}$ in the white region. This figure was reproduced with permission from Adachi et al. © 2017 IEEE. Reprinted with permission from DOI: https://doi.org/10.1109/TASC.2016.2631422. (For interpretation of the references to color in this figure legend, the reader is referred to the web version of this article.)

2.4. Visualization of current distribution

Unit gain constraint recursively applied null-steering spatial filtering (UGRENS) (Kumihashi and Sekihara, 2010; Sekihara and Nagarajan, 2015) was adapted to the acquired magnetic field data to reconstruct the temporal and spatial distribution of the equivalent currents after median and ulnar nerve stimulation in the region of interest (ROI). The ROI was defined as a flat area 50 mm above the top of the sensor array (area of the X-ray image in Fig. 2a; the black line in Fig. 2b). This distance was chosen because the distance between the sensor surface and the anterior margin of the C7 vertebra was almost 50 mm in most cases. The reconstructed currents at each acquisition time were superimposed on the X-ray image to visualize their distribution and intensity (Fig. 4). In this method, the current waveforms at arbitrary points in the ROI can be calculated as if virtual electrodes were placed there.

2.5. Comparison of current expansions

The current flowing into the cervical intervertebral foramen was calculated on the line connecting the midpoints of the right intervertebral joints of C4 and T2 (Line A, the black line in Fig. 5a). The conduction pathways of reconstructed currents near the clavicle were estimated from the spatial transition of the maximum intensity of the leading component of the reconstructed current (the dotted black line in Fig. 5a). The cross point of the conduction pathway and the clavicle was assumed to be the origin, and a line passing through the origin and perpendicular to the conduction pathway was set as Line B (the white line in Fig. 5a). The currents on Line B directing toward the spinal canal along the conduction pathway (the dotted black line in Fig. 5a) were calculated. The reconstructed currents after the median and ulnar nerve stimulations were compared to evaluate their expansion on either Line A or Line B. Lines A and B have the same length.

2.6. Evaluation of current waveforms

Virtual electrodes were set along the conduction pathway (the black lines in Fig. 6a and d) at 15-mm intervals (black-rimmed white circles in Fig. 6a and d). Waveforms of currents at each virtual electrode were respectively calculated by UGRENS (Fig. 6b and e). The conduction velocity was calculated from the peak latencies of the current waveforms from two virtual electrodes,

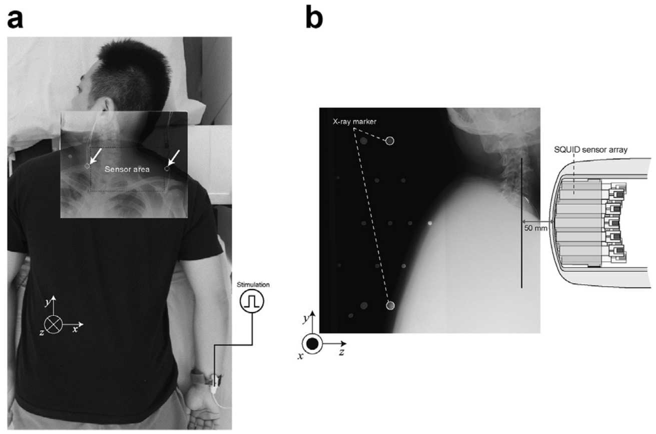

Fig. 2. (a) The subject was in the prone position on a table in a magnetically shielded room. The sensor area was arranged so as to cover the anterior neck to the coracoid process. An X-ray image is superimposed on that of the subject. The small circles in the X-ray image represent marker coils (white arrows). The relative position of the marker coils to the sensor array was obtained by recording the magnetic fields generated by the marker coils. A stimulator is on the ulnar nerve at the wrist in this figure. (b) Lateral view of the X-ray image in the measurement position. Two X-ray markers are indicated by white circles. The relative positions of the X-ray markers to the sensor array were measured in advance, and then the relative position of the subject to the sensor array in the X-ray image was obtained. Because the distance between the center of the sensor array and the anterior margin of the C7 vertebra was almost 50 mm in most cases, this was used as a depth parameter for equivalent current reconstruction. This figure was reproduced with permission from Adachi et al. © IOP Publishing. Reprinted with permission from DOI: https://doi.org/10.1088/1361-6668/aa66b3.

Nos. 3 and 5, set proximal to the clavicle (Fig. 6a and d). Similarly, the gray-rimmed white circles in Fig. 6a and d are virtual electrodes recording currents perpendicularly flowing toward the conduction pathway. These circles are 20 mm away from the conduction pathway. Furthermore, the current waveforms at the virtual electrode closest to Erb's point (electrode No. 4) and CNAP at Erb's point (the black dotted circle) were compared to evaluate the correspondence between the latencies of the reconstructed currents and CNAPs (Fig. 7).

3. Results

3.1. Recording of neuromagnetic fields and visualization of the equivalent current distribution in response to electrical stimulation of the median and ulnar nerves

Neuromagnetic fields above the clavicle and neck region were successfully recorded in response to stimulation of the median and ulnar nerves at the wrist in all subjects. Fig. 3 shows the evoked magnetic fields of a representative recording from the X-, Y-, and Z-directed coils (X, red; Y, green; Z, black; (b) median nerve; (c) ulnar nerve). Similarly, the same subject is shown in Figs. 3, 4, and 6. The peak-to-peak amplitudes of the magnetic fields from all coils were 195–420 fT after the median nerve stimulation and 100–180 fT after the ulnar nerve stimulation. The magnetic fields recorded from the coils of all directions showed two or three phasic waveforms and conducted from distal to proximal.

The equivalent currents after the median/ulnar nerve stimulation reconstructed by UGRENS were illustrated in a pseudocolor map and superimposed on the X-ray image (Fig. 4). First, the leading component of the equivalent current (represented by the large red arrow) appeared from medial and distal to the coracoid process and propagated toward the intervertebral foramina crossing the coracoid process (Fig. 4a: median nerve, 8.200–10.000 ms;

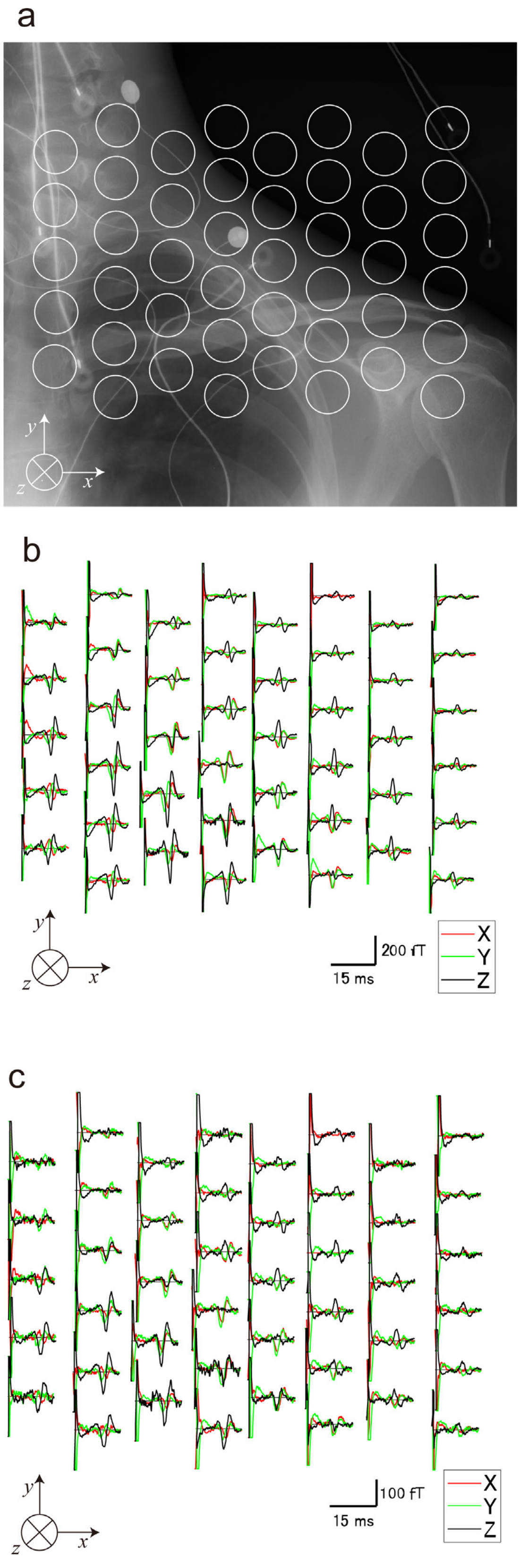

Fig. 3. (a) Relative position of the subject to each sensor bobbin. The X-ray image shows the cervical to shoulder region of the subject and the marker coils and electrodes. (b) and (c) Waveforms of magnetic fields measured in each sensor after (b) the median nerve stimulation and (c) the ulnar nerve stimulation in a representative case. Each waveform shows magnetic fields recorded from each sensor (X, red; Y, green; Z, black). One of the Y sensors was not working.

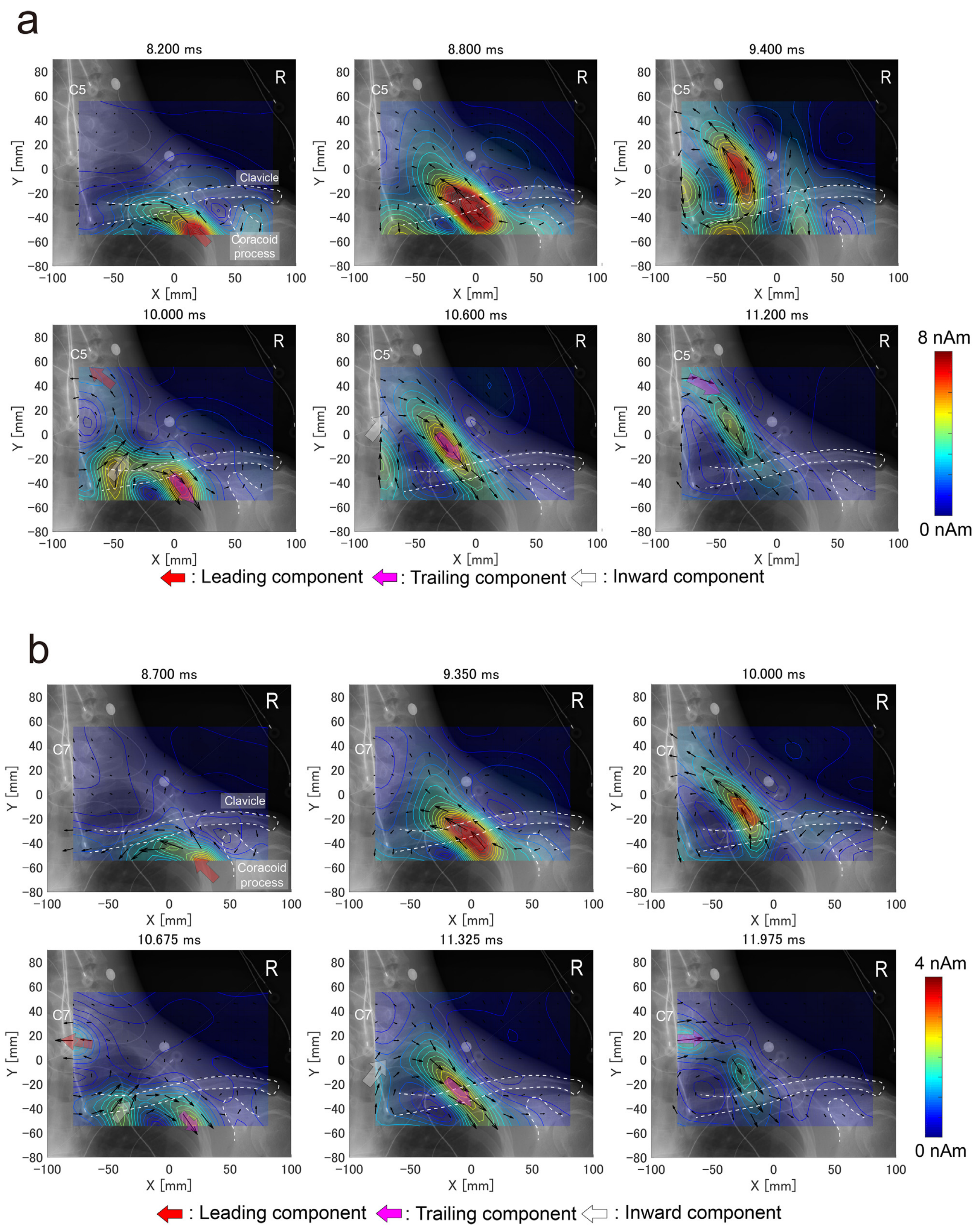

Fig. 4. Time course of the spatial distribution of equivalent currents in a representative case. The equivalent current densities are illustrated as a pseudocolor map superimposed on the X-ray image. Small black arrows indicate the direction of current at each position. (a) Equivalent currents in response to the median nerve stimulation. From 8.200 ms to 10.000 ms, the leading components appeared from the medial and distal directions to the coracoid process (large red arrow) and propagated toward the intervertebral foramina crossing the clavicles. From 10.000 ms to 11.200 ms, the trailing components appeared and similarly propagated (large pink arrow). From 9.400 ms to 10.600 ms, currents flowing toward the conduction pathway (white arrow) appeared from the medial side. (b) Equivalent currents in response to the ulnar nerve stimulation. The leading components (large red arrow) appeared and propagated cranially (from 8.700 ms to 10.675 ms). The trailing components (pink arrow) and currents flowing toward the conduction pathway (white arrow) appeared and similarly propagated (from 10.675 to 11.975 ms).

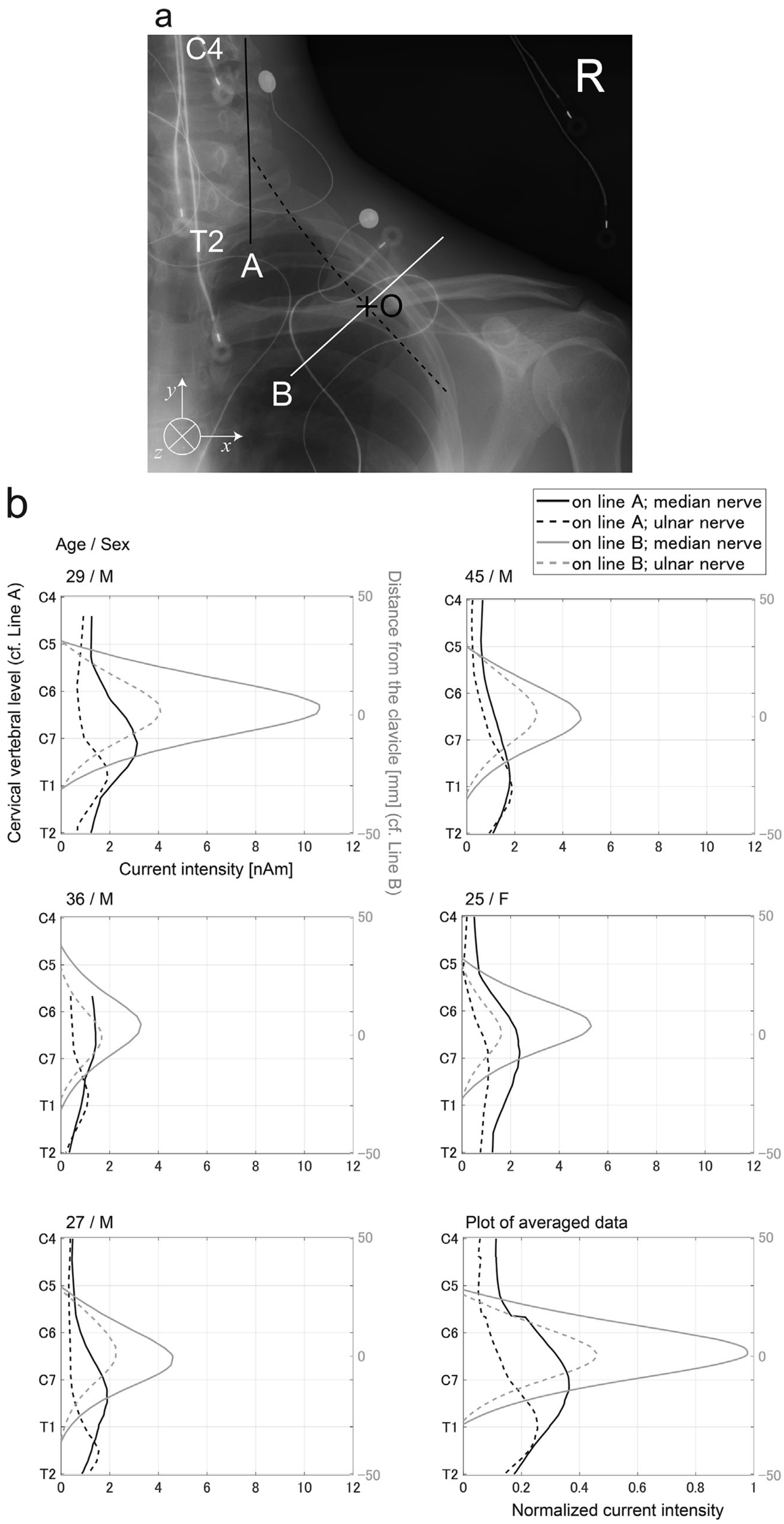

Fig. 5. Expansion of equivalent currents around the vertebral foramina and the clavicle. (a) Line A was defined as a line connecting the midpoints of the right intervertebral joint of C4 and that of T2. The cross point of the conduction pathway (the black dotted line) and the clavicle was set as the origin (O), and Line B (the white line) passes through the origin and perpendicular to the conduction pathway. The length of Line B is the same as that of Line A. (b) The current intensity on Lines A and B in response to electrical stimulation of the median and ulnar nerves in five subjects. The black solid and dotted lines are the current intensity on Line A after the median and ulnar nerve stimulations, respectively. The left-hand axis shows the position of the midpoint of the vertebral facet. The gray solid and dotted lines show the current intensity on Line B and the right-hand axis is the distance from the origin on the clavicle. The current intensity is on the axis of the abscissa. Solid lines, the median nerve stimulation; dotted lines, the ulnar nerve stimulation. The chart in the bottom right corner shows the averaged data of the five subjects as the peak latencies of the respective cases were normalized to 1.0.

Fig. 4b: ulnar nerve, 8.700–10.675 ms). Similarly, the trailing components of the equivalent currents (the large pink arrow) appeared and propagated toward the spinal canal (Fig. 4a: median nerve, 10.000–11.200 ms; Fig. 4b: ulnar nerve, 10.675–11.975 ms). Between the leading and trailing components, inward currents flowing into the conduction pathway (the large white arrow) appeared and propagated proximally (Fig. 4a: median nerve, 9.400–11.200 ms; Fig. 4b: ulnar nerve, 10.675–11.975 ms). The equivalent currents after the median nerve stimulation mainly flowed into C6/7–C7/T1, whereas the currents evoked by the ulnar nerve stimulation flowed into about C7/T1–T1/2.

3.2. Evaluation of the equivalent current distribution

The current intensities and expansion on Line A and Line B were compared among the five subjects (Fig. 5). The solid lines (for the median nerve stimulation) and interrupted lines (for the ulnar nerve stimulation) in Fig. 5b represent the distributions of the equivalent current intensities propagating across Line A and Line B in Fig. 5a. The left-hand vertical axis in Fig. 5b shows the level of the midpoint of the intervertebral body for evaluating the current expansion on Line A. The right-hand vertical axis shows the distance from the origin on the clavicle for gray plots. The chart in the bottom right corner represents the normalized data of the five subjects when the peak current intensity in each case was converted to 1.0.

The equivalent currents after the median nerve stimulation were mainly propagated into the C5/C6 to C7/T1 intervertebral foramina in the five subjects and peaked at C7 in the averaged chart (waveform depicted with a black solid line in Fig. 5b). In contrast, the reconstructed currents after the ulnar nerve stimulation propagated into the C6/C7 to T1/T2 intervertebral foramina and peaked at Th1 in the averaged chart (the black dotted line in Fig. 5b). The maximal intensity of the reconstructed currents on Line B (the currents directed toward the spinal canal) was almost located at the origin (gray solid and dotted lines in Fig. 5b). In addition, the current distributions on Line A (black waveforms in Fig. 5b) spread more widely than those on Line B (gray waveforms in Fig. 5b).

A paired t-test showed a significant difference in the positions of the peak current intensity on Line A between the median nerve stimulation and the ulnar nerve stimulation ($n = 5$, $p = 0.022$).

3.3. Evaluation of current waveforms

As shown in Fig. 6, the peaks of the leading components of the reconstructed currents (black upward waveforms in Fig. 6b and e) and the currents flowing into the conduction pathway (gray upward waveforms in Fig. 6b and e) propagated from distal to proximal in both the median and ulnar nerve stimulations.

In all subjects, the conduction velocities could be calculated from the upward peak latencies of the leading component of the reconstructed current at virtual electrodes Nos. 3 and 5 (Fig. 6b and e). The conduction velocities after median nerve stimulation and after ulnar nerve stimulation were 71.74 ± 6.67 m/s (mean ± SD, n = 5) and 71.82 ± 7.50 m/s (mean ± SD, n = 5), respectively.

Furthermore, currents perpendicularly flowing toward the conduction pathway at each virtual electrode could be reconstructed (gray waveforms in Fig. 6b and e). These virtual electrodes were set 20 mm medial from the conduction pathway (gray-rimmed white circles in Fig. 6a and d). The gray waveforms obtained at the virtual electrode closest to Erb's point (virtual electrode No. 4 in Fig. 6a and d) corresponded to the waveforms of CNAPs at Erb's point (dotted waveforms in Fig. 6c and f). The peak latencies of CNAPs at Erb's point were 10.158 ± 0.185 ms after the median nerve stimulation and 10.814 ± 0.337 ms after the ulnar nerve stimulation (mean of the difference, 0.656 ms). The peak latencies of the reconstructed equivalent currents were 10.115 ± 0.342 ms and 10.640 ± 0.457 ms, respectively (mean of the difference, 0.525 ms). The correlation between the peak latencies of the gray waveforms at the gray-rimmed electrode (No. 4) and CNAPs at Erb's point is shown in Fig. 7. The reconstructed currents flowing toward the conduction pathway and CNAPs showed a high linear correlation (cross, median nerve; circle, ulnar nerve; $y = x$; $R^2 = 0.8387$).

4. Discussion

MNG of the peripheral nerves and spinal cord is a new functional imaging modality that is currently under development. Our group has been working on the clinical application of MNG and believes that it is now feasible.

Notably, MNG can computationally reconstruct equivalent currents and visualize electrical activity. It helps clinicians, including non-specialists of neurology, understand spatiotemporal neurological activity, especially for deep-seated nerves such as the brachial plexus, spinal cord, and spinal nerves. In traditional neurophysiological examinations, conduction block cannot be observed before Wallerian degeneration when both stimulation and recording sites are located distal to the lesion site, whereas SEP can detect preganglionic brachial plexus injury. MNG can detect the lesion site before Wallerian degeneration because it can visualize neural activity conducting proximally through the lesion site. In brachial plexus injury, examination at an early stage may not be necessary in most cases, but it could provide new neurophysiological insight into the pathology of brachial plexus disorder.

As shown in Fig. 3, evoked neuromagnetic fields were larger in amplitude at the medial side of the scan area, especially near the anatomical position of the brachial plexus. The peak-to-peak amplitudes of the evoked magnetic fields were larger for median nerve stimulation than for ulnar nerve stimulation. The CNAPs at Erb's point showed a similar tendency in amplitude (Fig. 6c and f).

In Fig. 4a and b, the leading and trailing components of the equivalent currents conducted from distal to proximal, and the distance between the peaks of the two components exceeded 80 mm. Although these currents are an integration of currents in different conduction pathways, these two components represent expansion of neural activity in the brachial plexus. In addition, the currents flowing into the space between the two components appeared from the left side (the white arrow in Fig. 4a and b). Considering their direction, these components are supposed to be volume currents flowing into the depolarization site. Because the right side of the pseudocolor map is outside the body, there are no obvious inflow currents at the right side.

Although the results in the median nerve and the ulnar nerve were generally similar, the equivalent currents after the median nerve stimulation mainly flowed into C6/7–C7/T1 (Fig. 4a, 9.400–11.200 ms), whereas the currents evoked by the ulnar nerve stimulation flowed into about C7/T1–T1/2 (Fig. 4b, 10.675–11.975 ms). These results indicate that MNG can visualize neural activity in the brachial plexus, including the currents flowing into the depolarization site, and differentiate the conduction pathways of neural activities evoked by the median and ulnar nerves.

To prove that MNG could detect the variation in the conduction pathways of the brachial plexus, we evaluated the expansion of the current distribution at the nearby vertebral foramina and clavicle (Fig. 5). As in Fig. 4a and b, there was a spatial difference between the median and ulnar nerve stimulations regarding the reconstructed current distribution to the nearby vertebral foramina. In the normalized chart, current distribution peaked at C7 after median nerve stimulation but at Th1 after ulnar nerve stimulation. In addition, a significant difference was observed in the peak current

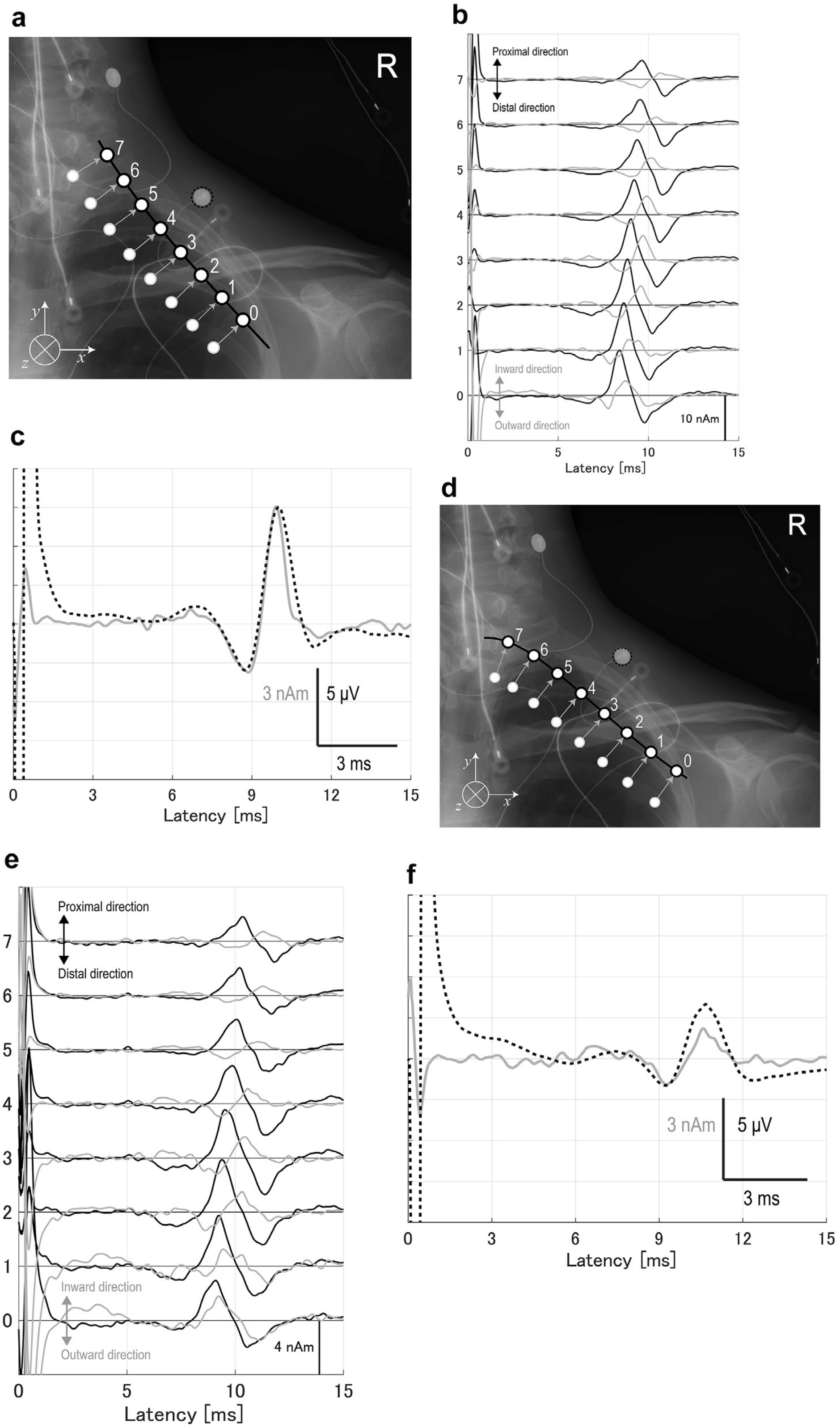

Fig. 6. (a) and (d) The black lines are the conduction pathways after (a) the median nerve and (d) the ulnar nerve stimulations, which are superimposed on the X-ray image. The black-rimmed circles represent virtual electrodes on the conduction pathways, and electrode No. 4 is closest to the electrode placed at Erb's point (black dotted circle). The gray-rimmed circles are virtual electrodes recording currents perpendicularly flowing into the conduction pathway. (b) and (e) Waveforms of equivalent currents conducting along the conduction pathway (black waveforms) and perpendicularly flowing into the conduction pathway (gray waveforms) after (b) the median nerve and (e) the ulnar nerve stimulations. The direction toward the spinal canal is upward in the black waveforms, and the direction toward the conduction pathway is upward in the gray waveforms. The conduction velocities were calculated from the peak latencies of the waveforms at virtual electrodes Nos. 3 and 5. (c) and (f) The dotted waveforms show CNAPs recorded from the electrodes at Erb's point (black dotted circles in Fig. 5a and d) referenced to the ear lobe. Upward in the dotted waveforms is negative in CNAPs. The gray waveforms represent the equivalent currents perpendicularly flowing into the conduction pathway at virtual electrode No. 4. Both waveforms have similar latency in (c) after the median nerve stimulation and (f) after the ulnar nerve stimulation.

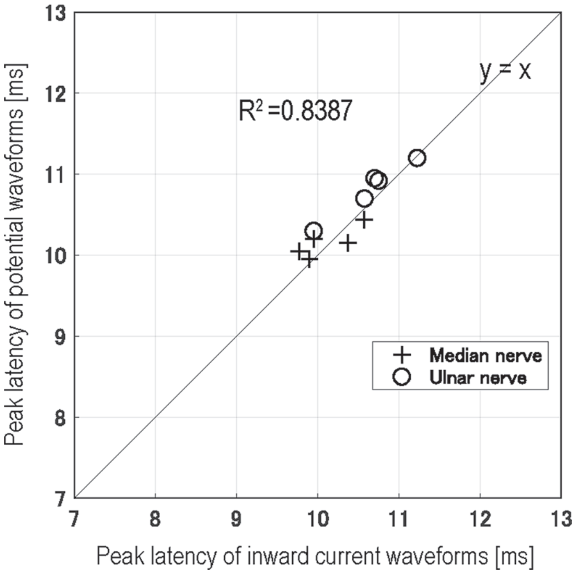

Fig. 7. Correlation between the peak latencies of CNAPs at Erb's point and inward currents flowing perpendicularly to the conduction pathway at the virtual electrodes closest to Erb's point (see the gray and black dotted waveforms in Fig. 6c and f). They showed high linear correlation (y = x; $R^2 = 0.8387$).

intensity on Line A between the median nerve stimulation and the ulnar nerve stimulation (n = 5, p = 0.022), though further research with a larger number of subjects is required. This discrepancy is consistent with the nerve root components of the median and ulnar nerves.

In contrast, the peak of the current intensity at the clavicle did not show a difference in position but only amplitude. This result corresponds with the anatomical characteristics of the brachial plexus, which is that the conduction pathways after the median and ulnar stimulations are located close to each other at the clavicle but are separate at the nearby vertebral foramina. Therefore, MNG has the potential to differentiate the conduction pathways in the brachial plexus.

In Fig. 6c and f, the peak of the reconstructed equivalent current flowing into the depolarization site at virtual electrode No. 4 (gray waveform) corresponded to the peak of the CNAP at Erb's point (black dotted waveform). Physiologically, the negative peak of the CNAP represents the depolarization site. Therefore, these results also indicate that the peak of the currents flowing toward the conduction pathway represent the currents flowing into the depolarization site. The results are not only consistent with physiological knowledge, but also with our early studies that illustrated the correspondence of action potentials, intra-axonal currents, and evoked magnetic fields (Fukuoka et al., 2004, 2002). For confirmation, we evaluated the peak latencies of the gray and black dotted waveforms in Fig. 6c and f using correlation analysis (Fig. 7). The results showed high linear correlation in both the median and ulnar nerve stimulations (y = x; $R^2 = 0.8387$).

In this study, the peak latencies of CNAPs and the reconstructed currents at Erb's point were 10–11 ms, and the differences between the median and ulnar nerves were about 0.50–0.66 ms. Ozaki et al. (1996) reported that the onset latency of the SEP at Erb's point (N9) was 8.1 ± 0.7 ms in the ulnar nerve and 7.7 ± 0.6 ms in the median nerve. In addition, the peak latencies were 8.9 ± 0.7 ms in the ulnar nerve and 8.6 ± 0.6 ms in the median nerve. Sonoo et al. (1996) noted that the mean onset latency of N9 by the median nerve was 7.96 ms and that the mean interval between the onset and peak of N9 was about 1.5 ms. Moreover, Tanosaki et al. (1999) reported that the mean onset latency of N9 was 7.41 ms and that the peak latency was 8.75 ms and that the onset latency correlated with age and height. Although the peak latencies of the CNAPs at Erb's point in this study were longer, this could be due to differences in the recording position and the position of the upper extremity. Desmedt et al. (1983) reported that SEPs change with shoulder position. In addition, the differences between the latencies of the median and ulnar nerves can be attributed to the difference in nerve lengths, as reported by Ozaki et al. (1996).

Although this study successfully visualized the spatiotemporal transition of neural activity in the brachial plexus, some limitations still remain. One potential drawback is the recording position of the subjects. In this study, the subjects were prone on the table with the neck rotated and arm pronated. However, rotation of the cervical spine for a long period is difficult and sometimes risky in elderly patients or patients with cervical spine morbidity. We need to improve the measurement position. The second limitation is the MNG resolution. Although we have shown that the reconstructed equivalent currents conducted and expanded consistently with the anatomical features of the brachial plexus, greater precision is required for differentiation of the currents in the roots, trunks, and cords. We will develop MNG further to boost its clinical application.

5. Conclusions

This study demonstrated that MNG visualizes neural activity in the brachial plexus and differentiates the conduction pathway of the median and ulnar nerve components. The pseudocolor map of the reconstructed equivalent currents showed that MNG could reconstruct not only the leading and trailing components of currents, but also the inward currents at the depolarization site. MNG could be a novel functional imaging modality for brachial plexus pathologies that is easily comprehensible even for physicians not specialized in neurology. This universally applicable diagnostic modality will be of great benefit for patients.

Funding

This research was funded by RICOH Company, Ltd.

Author contributions

T.W., S.K., and A.O. took part in the conception and design of the project; T.W., W.K., S.U., T.S., Y.M, and Y.A. were involved in its execution; and T.W., Y.H., S.K., Y.M., I.O., Y.A., and K.S. carried out analysis and interpretation of data. All authors have approved the submission of this manuscript.

Declaration of Competing Interest

The authors declared that there is no conflict of interest.

References

Adachi Y, Kawabata S, Fujihira J, Uehara G. Multi-channel SQUID magnetospinogram system with closed-cycle helium recondensing. IEEE Trans Appl Supercon 2017;27:1600604.
Adachi Y, Kawai J, Miyamoto M, Ogata H, Tomori M, Kawabata S, et al. A SQUID system for measurement of spinal cord evoked field of supine subjects. IEEE Trans Appl Supercon 2009;19:861–6.
Adachi Y, Kawai J, Uehara G, Miyamoto M, Tomizawa S, Kawabata S. A 75-ch SQUID biomagnetometer system for human cervical spinal cord evoked field. IEEE Trans Appl Supercon 2007;17:3867–73.
Adachi Y, Miyamoto M, Kawai J, Uehara G, Ogata H, Kawabata S, et al. Improvement of SQUID magnetometer system for extending application of spinal cord evoked magnetic field measurement. IEEE Trans Appl Supercon 2011;21:485–8.

Adachi Y, Oyama D, Kawai J, Kawabata S, Uehara G. Spinal cord evoked magnetic field measurement using a magnetospinography system equipped with a cryocooler. Conf Proc IEEE Eng Med Biol Soc 2013;2013:4426–9.

Caranci F, Briganti F, La Porta M, Antinolfi G, Cesarano E, Fonio P, et al. Magnetic resonance imaging in brachial plexus injury. Muscul Surg 2013;97:S181–90.

Curio G, Erné SN, Sandfort J, Scheer J, Stehr R, Trahms L. Exploratory mapping of evoked neuromagnetic activity from human peripheral nerve, brachial plexus and spinal cord. Electroencephalogr Clin Neurophysiol 1991;81:450–3.

Desmedt JE, Nguyen TH, Carmeliet J. Unexpected latency shifts of the stationary P9 somatosensory evoked potential far field with changes in shoulder position. Electroencephalogr Clin Neurophysiol 1983;56:628–34.

Erne SN, Narici L, Pizzella V, Romani G. The positioning problem in biomagnetic measurements: a solution for arrays of superconducting sensors. IEEE Trans Magn 1987;23:1319–22.

Ferrante MA. Electrodiagnostic assessment of the brachial plexus. Neurol Clin 2012;30:551–80.

Fukuoka Y, Komori H, Kawabata S, Ohkubo H, Shinomiya K. Visualization of incomplete conduction block by neuromagnetic recording. Clin Neurophysiol 2004;115:2113–22.

Fukuoka Y, Komori H, Kawabata S, Ohkubo H, Shinomiya K, Terasaki O. Imaging of neural conduction block by neuromagnetic recording. Clin Neurophysiol 2002;113:1985–92.

Giuffre JL, Kakar S, Bishop AT, Spinner RJ, Shin AY. Current concepts of the treatment of adult brachial plexus injuries. J Hand Surg Am 2010;35:678. 88 quiz 688.

Hashimoto I, Odaka K, Gatayama T, Yokoyama S. Multichannel measurements of magnetic compound action fields of the median nerve in man. Electroencephalogr Clin Neurophysiol 1991;81:332–6.

Hoshino Y, Kawabata S, Komori H, Ohkubo H, Tomizawa M, Shinomiya K. Three-dimensional neuromagnetic recording in the spinal cord. Int Cong Ser 2005;1278:309–12.

Hoshiyama M, Kakigi R, Nagata O. Peripheral nerve conduction recorded by a micro gradiometer system (micro-SQUID) in humans. Neurosci Lett 1999;272:199–202.

Ishii S, Kawabata S, Tomizawa S, Tomori M, Sakaki K, Shinomiya K, et al. Conductive neuromagnetic fields in the lumbar spinal canal. Clin Neurophysiol 2012;123:1656–61.

Kawabata S, Komori H, Mochida K, Harunobu O, Shinomiya K. Visualization of conductive spinal cord activity using a biomagnetometer. Spine 2002;27:475–9.

Klein A, van Leeuwen P, Hoormann J. Magnetoneurographic registration of propagating magnetic fields in the lumbar spine after stimulation of the posterior tibial nerve. J Neural Eng 2006;3:125–31.

Kumihashi I, Sekihara K. Array-gain constraint minimum-norm spatial filter with recursively updated gram matrix for biomagnetic source imaging. IEEE Trans Biomed Eng 2010;57:1358–65.

Mackert BM. Magnetoneurography: theory and application to peripheral nerve disorders. Clin Neurophysiol 2004;115:2667–76.

Mackert BM, Burghoff M, Hiss LH, Nordahn M, Marx P, Trahms L, et al. Magnetoneurography of evoked compound action currents in human cervical nerve roots. Clin Neurophysiol 2001a;112:330–5.

Mackert BM, Burghoff M, Hiss LH, Nordahn M, Trahms L, Curio G. Non-invasive magnetoneurography for 3D-monitoring of human compound action current propagation in deep brachial plexus. Neurosci Lett 2000;289:33–6.

Mackert BM, Burghoff M, Hiss LH, Trahms L, Curio G. Tracing of proximal lumbosacral nerve conduction–a comparison of simultaneous magneto- and electroneurography. Clin Neurophysiol 2001b;112:1408–13.

Mackert BM, Curio G, Burghoff M, Marx P. Mapping of tibial nerve evoked magnetic fields over the lower spine. Electroencephalogr Clin Neurophysiol 1997;104:322–7.

Mackert BM, Curio G, Burghoff M, Trahms L, Marx P. Magnetoneurographic 3D localization of conduction blocks in patients with unilateral S1 root compression. Electroencephalogr Clin Neurophysiol 1998;109:315–20.

Marquez Neto OR, Leite MS, Freitas T, Mendelovitz P, Villela EA, Kessler IM. The role of magnetic resonance imaging in the evaluation of peripheral nerves following traumatic lesion: where do we stand? Acta Neurochir 2017;159:281–90.

O'Shea K, Feinberg JH, Wolfe SW. Imaging and electrodiagnostic work-up of acute adult brachial plexus injuries. J Hand Surg Eur 2011;36:747–59.

Ohkubo H, Komori H, Kawabata S, Fukuoka Y, Shinomiya K. Estimation of localization of neural activity in the spinal cord using a biomagnetometer. J Med Dent Sci 2003;50:177–82.

Ozaki I, Takada H, Shimamura H, Baba M, Matsunaga M. Central conduction in somatosensory evoked potentials: comparison of ulnar and median data and evaluation of onset versus peak methods. Neurology 1996;47:1299–304.

Rehman I, Chokshi FH, Khosa F. MR imaging of the brachial plexus. Clin Neuroradiol 2014;24:207–16.

Sekihara K, Nagarajan SS. Electromagnetic brain imaging: a Bayesian perspective. Springer International Publishing; 2015.

Simon NG, Spinner RJ, Kline DG, Kliot M. Advances in the neurological and neurosurgical management of peripheral nerve trauma. J Neurol Neurosurg Psychiatr 2016;87:198–208.

Sonoo M, Kobayashi M, Genba-Shimizu K, Mannen T, Shimizu T. Detailed analysis of the latencies of median nerve somatosensory evoked potential components, 1: selection of the best standard parameters and the establishment of noramal values. Clin Neurophysiol 1996;100:319–31.

Sumiya S, Kawabata S, Hoshino Y, Adachi Y, Sekihara K, Tomizawa S, et al. Magnetospinography visualizes electrophysiological activity in the cervical spinal cord. Sci Rep 2017;7:2192.

Tanosaki M, Ozaki I, Shimamura H, Baba M, Matsunaga M. Effects of aging on central conduction in somatosensory evoked potentials: evaluation of onset versus peak methods. Clin Neurophysiol 1999;10:2094–103.

Tomizawa S, Kawabata S, Komori H, Hoshino Fukuoka Y, Shinomiya K. Evaluation of segmental spinal cord evoked magnetic fields after sciatic nerve stimulation. Clin Neurophysiol 2008;119:1111–8.

Tomori M, Kawabata S, Tomizawa S, Ishii S, Enomoto M, Adachi Y, et al. Diagnosis of incomplete conduction block of spinal cord from skin surface using spinal cord evoked magnetic fields. J Orthop Sci 2010;15:371–80.

Trahms L, Erné SN, Trontelj Z, Curio G. Biomagnetic functional localization of a peripheral nerve in man. Biophys J 1989;55:1145–53.

Ushio S, Hoshino Y, Kawabata S, Adachi Y, Sekihara K, Sumiya S, et al. Visualization of the electrical activity of the cauda equina using a magnetospinography system in healthy subjects. Clin Neurophysiol 2019;130:1–11.

Wijesinghe RS. Magnetic measurements of peripheral nerve function using a neuromagnetic current probe. Exp Biol Med 2010;235:159–69.

Wijesinghe RS. Detection of magnetic fields created by biological tissues. J Electr Electron Syst 2014;3:120.

Wijesinghe RS, Roth BJ. Detection of peripheral nerve and skeletal muscle action currents using magnetic resonance imaging. Ann Biomed Eng 2009;37:2402–6.

Wikswo JP, Barach JP, Freeman JA. Magnetic field of a nerve impulse: first measurements. Science 1980;208:53–5.